Check for updates

Geochemistry, Geophysics, Geosystems®

AGU ADVANCING EARTH AND SPACE SCIENCES

RESEARCH ARTICLE
10.1029/2024GC011559

Ultra-Low Velocity Zone Beneath the Atlantic Near St. Helena

Felix Davison[1], Carl Martin[1,2], Rita Parai[3], and Sanne Cottaar[1]

[1]Department of Earth Sciences, University of Cambridge, Cambridge, UK, [2]Faculty of Geosciences, Utrecht University, Utrecht, The Netherlands, [3]Department of Earth, Environmental, and Planetary Sciences, Washington University in St. Louis, St. Louis, MO, USA

Key Points:

- Observation of significant S_{diff} postcursors sampling the CMB beneath the Atlantic
- Modeling of postcursors reveals a previously unknown mega-ULVZ situated on the CMB to the West of St. Helena
- Further measurements of St. Helena and Ascension samples are needed to identify a potential ULVZ-associated geochemical signature

Supporting Information:

Supporting Information may be found in the online version of this article.

Correspondence to:

F. Davison,
fpd21@cam.ac.uk

Citation:

Davison, F., Martin, C., Parai, R., & Cottaar, S. (2024). Ultra-low velocity zone beneath the Atlantic near St. Helena. *Geochemistry, Geophysics, Geosystems*, *25*, e2024GC011559. https://doi.org/10.1029/2024GC011559

Received 11 MAR 2024
Accepted 21 JUN 2024

Author Contributions:

Conceptualization: Carl Martin, Sanne Cottaar
Data curation: Felix Davison, Carl Martin
Formal analysis: Felix Davison
Funding acquisition: Sanne Cottaar
Investigation: Felix Davison, Carl Martin, Rita Parai
Methodology: Felix Davison, Sanne Cottaar
Project administration: Sanne Cottaar
Resources: Sanne Cottaar
Supervision: Carl Martin, Sanne Cottaar
Visualization: Felix Davison
Writing – original draft: Felix Davison, Rita Parai, Sanne Cottaar

© 2024 The Author(s). Geochemistry, Geophysics, Geosystems published by Wiley Periodicals LLC on behalf of American Geophysical Union.
This is an open access article under the terms of the Creative Commons Attribution License, which permits use, distribution and reproduction in any medium, provided the original work is properly cited.

Abstract There are various hotspots in the Atlantic Ocean, which are underlain by mantle plumes that likely cross the mantle and originate at the core-mantle boundary. We use teleseismic core-diffracted shear waves to look for an Ultra-Low Velocity Zone (ULVZ) at the potential base of central Atlantic mantle plumes. Our data set shows delayed postcursory phases after the core-diffracted shear waves. The observed patterns are consistent in frequency dependence, delay time, and scatter pattern with those caused by mega-ULVZs previously modeled elsewhere. Synthetic modeling of a cylindrical structure on the core-mantle boundary below St. Helena provides a good fit to the data. The preferred model is 600 km across and 20 km high, centered at approximately 15° South, 15° West, and with a 30% S-wave velocity reduction. Significant uncertainties and trade-offs do remain to these parameters, but a large ULVZ is needed to explain the data. The location is west of St. Helena and south of Ascension. Helium and neon isotopic systematics observed in samples from this region could point to a less-outgassed mantle component mixed in with the dominant signature of recycled material. These observations could be explained by a contribution from the Large Low Shear Velocity Province (LLSVP). Tungsten isotopic measurements would be needed to understand whether a contribution from the mega-ULVZ is also required at St. Helena or Ascension.

Plain Language Summary Nearly 3,000 km beneath the Atlantic to the West of the island of St. Helena, on the boundary between Earth's metal core and rocky mantle, we have discovered a new area where seismic waves diffracting along that boundary travel significantly slower than expected. This area is called an ultra-low velocity zone. In this study, we use seismic waves which propagate along the core-mantle boundary. The waves that interact with the ultra-low velocity zone are scattered and become severely delayed. Using the observations, we have constrained the ultra-low velocity zone to a broadly cylindrical structure, 600 km across, 20 km high and centered at 15° South, 15° West. The material inside is reduced by 30% in seismic shear wave velocity compared to outside. We confirmed this model by computing and comparing synthetic waveforms for a range of different ultra-low velocity zone models. This ULVZ location is right beside or just inside a much larger region of low velocity, dubbed the African Large Low Shear-Velocity Province (LLSVP). The observed ultra-low velocity zone could be the base of the upwelling or mantle plume rising through the mantle and causing the hotspots of St. Helena and/or Ascension at the surface.

1. Introduction

The core-mantle boundary (CMB) is both an area of significance in mantle dynamics—being the lower thermal boundary layer in mantle convection—and a region of great lateral heterogeneity as observed by seismology. This heterogeneity is most notable in the two antipodal large low shear-velocity provinces (LLSVPs) extending upwards as far as 1,000 km at the highest point (e.g., Cottaar & Lekic, 2016)—one beneath the Pacific and one beneath Africa. Beyond these comparatively well-imaged structures, scattered smaller-scale heterogeneities—tens of kilometers high, and hundreds across—with extreme velocity reductions are found and dubbed Ultra-Low Velocity Zones (ULVZs) (e.g., Yu & Garnero, 2018). A number of ULVZs—including the largest of those modeled in 3D—have been found at or near the base of major mantle plumes, specifically those underlying the Hawaiian (Cottaar & Romanowicz, 2012; Jenkins et al., 2021; Lai et al., 2022; J. Li et al., 2022; Z. Li et al., 2022; Martin et al., 2023a), Icelandic (Yuan & Romanowicz, 2017), Samoan (Krier et al., 2021; Thorne et al., 2013), and Galápagos (Cottaar et al., 2022) hotspots.

Writing – review & editing: Felix Davison, Carl Martin, Rita Parai, Sanne Cottaar

While the composition and internal structure of ULVZs remains uncertain, their extreme velocity reductions imply that they must have anomalous compositions. One candidate is magnesiowüstite enrichment (e.g., Dobrosavljevic et al., 2019), and another is the presence of partial melt (e.g., Dannberg et al., 2021; Kimura et al., 2017; Lay et al., 2004). The consistent association of the well-characterized "mega-ULVZs"—Hawaii, Iceland, Samoa and Galápagos—with isotopic anomalies in the ocean island basalts (e.g., Jackson et al., 2017; Mundl et al., 2017) implies the ULVZs might have either a primordial origin or had significant chemical exchange with the core (Mundl-Petermeier et al., 2020).

Many more ULVZs are mapped beneath the Pacific Ocean, and are potentially associated with the Pacific LLSVP, compared to the region beneath Africa and the Atlantic, which could be associated with the African LLSVP (e.g., compilation in Yu and Garnero (2018)). This difference could be due to less optimal earthquake-station geometries targeting the core-mantle boundary beneath the Atlantic and Africa. Up to now, there has been one mega-ULVZ mapped at the northern edge of the African LLSVP beneath Iceland (Yuan & Romanowicz, 2017). Evidence of presence of ULVZs is found further south and west within and around the edges of the LLSVP (Helmberger et al., 2000; Ni & Helmberger, 2001a, 2001b; Thorne et al., 2021; Wen, 2000). There are a number of volcanic hotspots across the Southern Atlantic that are thought to be underlain by whole mantle plumes (S. W. French & Romanowicz, 2015; Marignier et al., 2020). Some of these hotspots (St. Helena, Ascension) carry a distinctive geochemical signature thought to reflect incorporation of ancient recycled oceanic crust in the source (HIMU, Chauvel et al., 1992; Zindler & Hart, 1986), but Ne systematics at such HIMU hotspots can still reveal a primordial components (X. J. Zhang et al., 2024). The question is open if these hotspots in the Atlantic could also linked to the presence of mega-ULVZs at or near their base.

Here we target a large swath of the CMB beneath the Atlantic south of the equator using shear diffracted (S_{diff}) body-waves. Diffracted waves along the core-mantle boundary are slowed significantly within a ULVZ and refracted at its edges, leading to a delayed secondary arrival or postcursor (Figure 1). The postcursory energy refracted by the ULVZ arrives at stations delayed and from a different angle. We find evidence of postcursors caused by a previously unmapped ULVZ at the CMB to the west of St. Helena. We use data from four principal earthquakes with varied azimuthal sensitivity to model the ULVZ in further detail. We compare with synthetic seismograms produced for a range of 3D cylindrical ULVZ models, to constrain its rough position, height, width, and velocity reduction.

2. Methods and Data

2.1. Data Catalog and Assessment

To distinguish S_{diff} postcursors from depth phases requires dense station coverage to observe the postcursor move-out as it varies with azimuth. Additionally, the ULVZ needs to be sampled from different azimuthal directions to be accurately located. As such, we considered three principal geometries which sample beneath the Atlantic around the equator: from Prince Edward Island to the East Coast of North America; from the South Sandwich islands to Western Europe; and from Peru to East Africa. We analyzed earthquakes over magnitude 5.7 at the correct distance range (95–135°) to sample the CMB. All 31 earthquakes examined in detail after a first-pass manual assessment of all events meeting those criteria are listed in Supporting Information S1. As the SV energy of S_{diff} converts readily to P-waves in the outer core, and therefore attenuates strongly along the CMB leg of the ray-path, we use the SH energy on the transverse component.

While prior studies of S_{diff} typically involved visual assessment of data for quality control (e.g., Cottaar et al., 2022), here we implement an automated and reproducible approach. Our algorithm exploits the fact that the postcursors move-out with time as a function of azimuth with respect to the main phase. Thus, the postcursor will stack coherently in local azimuth bins, but not across wide azimuth bins. Our algorithm follows the following steps for each event:

1. Data are filtered between 10 and 35 s.
2. Data are windowed between −20 and 100 s before and after the predicted S_{diff} phase arrival.
3. We create bins of waveforms for each degree azimuth, and create linear stacks within each bin. This is referred to as the "local" stack.
4. A linear stack of all waveforms in a densely sampled area is created using all waveforms that correlate strongly (>0.8) with their "local" stack. We refer to this as the "global" stack.

15252027, 2024, 7, Downloaded from https://agupubs.onlinelibrary.wiley.com/doi/10.1029/2024GC011559 by Washington University School Of Medicine, Wiley Online Library on [02/05/2025]. See the Terms and Conditions (https://onlinelibrary.wiley.com/terms-and-conditions) on Wiley Online Library for rules of use; OA articles are governed by the applicable Creative Commons License

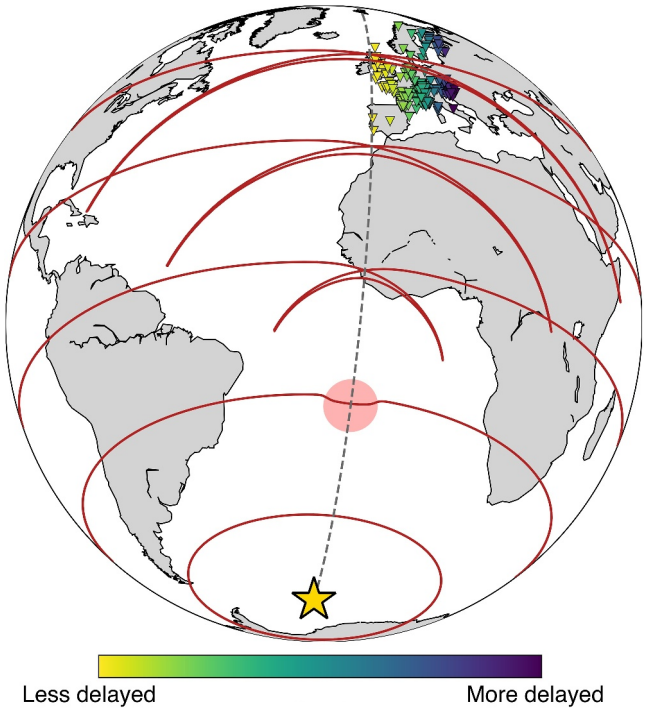

Figure 1. A series of wavefronts passing through a model ULVZ. Geometry is for a ULVZ near St. Helena and an earthquake at the South Sandwich Islands recorded at stations across Europe. The arcuate shape of the postcursor means it will arrive later at stations further from the event-ULVZ axis (dashed line).

5. To ensure a good signal-to-noise ratio, waveforms with less than 0.2 correlation to the global stack are rejected.
6. Each remaining waveform that correlates more with the global stack than the local stack is rejected, unless the correlation coefficient with either the local or the global stack exceeds 0.8.

The exception to the final rule is to reduce the loss of high-quality traces without a postcursor, which might correlate well to the global stack, and thus the loss of high-quality traces with no clear postcursor. Visual examples of the waveforms we accept and reject are included in Supporting Information S1. Our algorithm offers advantages in ease-of-use and scalability, and requires minimal tuning. Advantages over "by-eye" assessment are in reproducibility, robustness, and speed.

After quality control, we select four comparatively high quality events covering the range of geometries shown in Figure 2 to model in further detail.

2.2. Synthetic Modeling

We produce synthetic seismograms using sandwiched-CSEM, the "sandwiched" version of the Coupled Spectral Element Method (Capdeville et al., 2003). In this method, a spectral element solution is calculated only for the lowermost 370 km of the mantle, with a normal mode solution used for both the core and the remainder of the mantle and crust. This allows us the implement the 3D structure of interest at the core-mantle boundary, while reducing computational cost such that we can compute synthetics for many models down to 10 s period; prior studies including Yuan and Romanowicz (2017) and Cottaar et al. (2022) have used the same method.

To simplify the model space down to a computationally tractable problem, we assume a cylindrical ULVZ, and attempt to find values for its radius, height, location and shear-wave velocity reduction. As the model space remains too broad for a full grid search of all parameters, we instead iterate by producing synthetic seismograms from a model, visually comparing move-out patterns, and updating the model accordingly to improve the fit.

Our background model within the 3D modeled region for shear wave velocity is SEMUCB-WM1 (S. French & Romanowicz, 2014). This tapers toward the background 1D model in the top 70 km of the SEM mesh. Inside the ULVZ, we reduce V_S according to the model in use. The choice of P-wave velocity and density in the ULVZ have negligible impact on the resultant waveforms; our model scales dV_P equally to dV_S, and density deviation by $-\frac{1}{2}$ dV_S, meaning the ULVZ is heavy. We present our best-fitting ULVZ in the main paper and illustrate trade-offs in Supporting Information S1.

3. Results

3.1. Data Set and Selected Earthquake Parameters

The four earthquakes we base our model on are outlined in Figure 2 and Table 1. Events A and B are in the Prince Edward Island region and their S_{diff} waves are recorded across the eastern United States, with the Transportable Array providing excellent coverage with azimuth to identify postcursors. While this geometry gives us dense, high quality observations, it is on its own not sufficient to locate the ULVZ. As such, events C and D—from the South Sandwich Islands to Europe and from Peru to East Africa, respectively—provide useful crossing ray path coverage to help constrain the location, as well as providing independent checks on the success of synthetic models.

Figures 3–6 show real and synthetic data for these events. Waveforms are centered on the predicted S_{diff} arrival time (for PREM, Dziewonski & Anderson, 1981) and filtered between 10 and 20 s period. Waveforms are organized by azimuth from their event, rounded to the nearest degree, to make the plots clearer. Interpreted postcursors are highlighted for each event and show a move-out as a function of azimuth.

15252027, 2024, 7, Downloaded from https://agupubs.onlinelibrary.wiley.com/doi/10.1029/2024GC011559 by Washington University School Of Medicine, Wiley Online Library on [02/05/2025]. See the Terms and Conditions (https://onlinelibrary.wiley.com/terms-and-conditions) on Wiley Online Library for rules of use; OA articles are governed by the applicable Creative Commons License

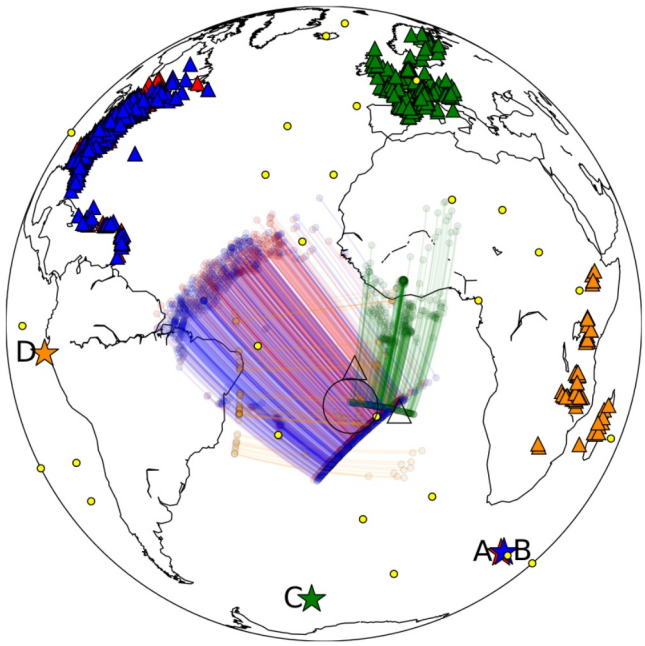

Figure 2. Map showing the coverage on the core-mantle boundary of S_{diff} raypaths. Stars are earthquake sources, labeled by event and triangles are receivers. Event A- red, event B- blue, event C- green, event D- orange. Colored circles mark pierce points where ray-paths enter and leave the core-mantle boundary, with colored lines between circles showing where the great circle ray paths are sensitive to the core-mantle boundary; note that scattered postcursory phases will follow different paths. Our preferred ULVZ model is shown as a circle, centered at 15°S, 15°W, and a radius of 300 km. Major hotspots are shown as yellow circles and the volcanic islands of Ascension and St. Helena are shown as triangles.

All four events occurred between depths of 12 and 21 km, and, due to this shallow origin, their depth phases arrive within the main wave train for this period band. The interpreted postcursors merge with the main wave train in events A, B, and D, and to a lesser degree in C. Shallow structure may well complicate the waveforms, but should introduce the same change into both the main phase and the postcursor. As a result, we do not expect postcursor move-out, delay time, or relative amplitude to be affected.

As S_{diff} arrivals are comprised of primarily SH energy, SH radiation patterns for each of the focal mechanisms A-D are included in Supporting Information S1. All four events have simple source time functions with one dominant peak (found using SCARDEC, Vallée et al., 2011).

3.2. Preferred Model Parameters

Two sets of synthetic data are also presented in Figures 3–6. One includes 3D velocity variations as in SEMCUCB for the lowermost mantle, and the other includes our best model ULVZ on top of the background model.

The model producing the best-fitting synthetics includes a cylindrical ULVZ centered at 15 ± 2°S, 15 ± 2°W with a diameter of 600 ± 150 km and a height of 20 ± 5 km. This width on the core-mantle boundary covers almost 10°. Within the ULVZ, V_S is reduced by 30% ± 5%.

Our preferred ULVZ demonstrates a cylindrical ULVZ can roughly explain the observed postcursors. This is likely not a unique model within our simplified model space. An exploration of models with varied parameters is included in Supporting Information S1 to illustrate the potential errors in the model. Changing the location by 4° shows a noticeable shift in the minimum travel time move-out for the postcursors (≥5 s). The larger and wider ULVZs increase the amplitudes and delay times of the S_{diff} postcursors, by on the order of 50% and 10 s respectively. Delay times are also affected by the choice of velocity reduction. There is a trade-off between size and velocity reduction resulting in comparable delay times for the postcursors, with a 10% reduction in V_S roughly compensating for a 10 km difference in ULVZ height.

As a result of the trade-offs between these parameters, their uncertainties are not independent. Owing to the high dimensionality of the model space, and the computational cost associated with generating synthetic data for one model, a full mapping of all possible parameter values was not feasible. Instead, we carried out a search of model space, iteratively updating one to two parameters at a time until the visual waveform fit no longer improved. Models explored ranged from −10% to −30% V_S in increments of 5%, 10–30 km in height in increments of 5 km, and from 4° South, 11° West to 19° South, 19° West in increments of 1–4°, with larger increments used when synthetic results were less accurate.

After settling on a model, we modified the preferred model by 4° in latitude or longitude, or with ±300 km diameter, or with ±10 km height, or with ±10% V_S reduction. These all produced a noticeably worse fit to data,

Table 1
Earthquake Source Parameters

	Date	Lon. (°E)	Lat. (°N)	M_W	Depth (km)	Location
A	2014/11/17	33.79	−46.27	6.2	17.6	Prince Edward Island
B	2013/07/22	34.93	−45.89	6.3	20.7	Prince Edward Island
C	2021/08/22	−23.60	−60.33	6.7	12.0	South Sandwich Islands
D	2013/08/12	−82.13	−5.52	6.2	12.0	Off Coast of Peru

Note. From the Global Centroid-Moment-Tensor project (Ekström et al., 2012).

15252027, 2024, 7, Downloaded from https://agupubs.onlinelibrary.wiley.com/doi/10.1029/2024GC011559 by Washington University School Of Medicine, Wiley Online Library on [02/05/2025]. See the Terms and Conditions (https://onlinelibrary.wiley.com/terms-and-conditions) on Wiley Online Library for rules of use; OA articles are governed by the applicable Creative Commons License

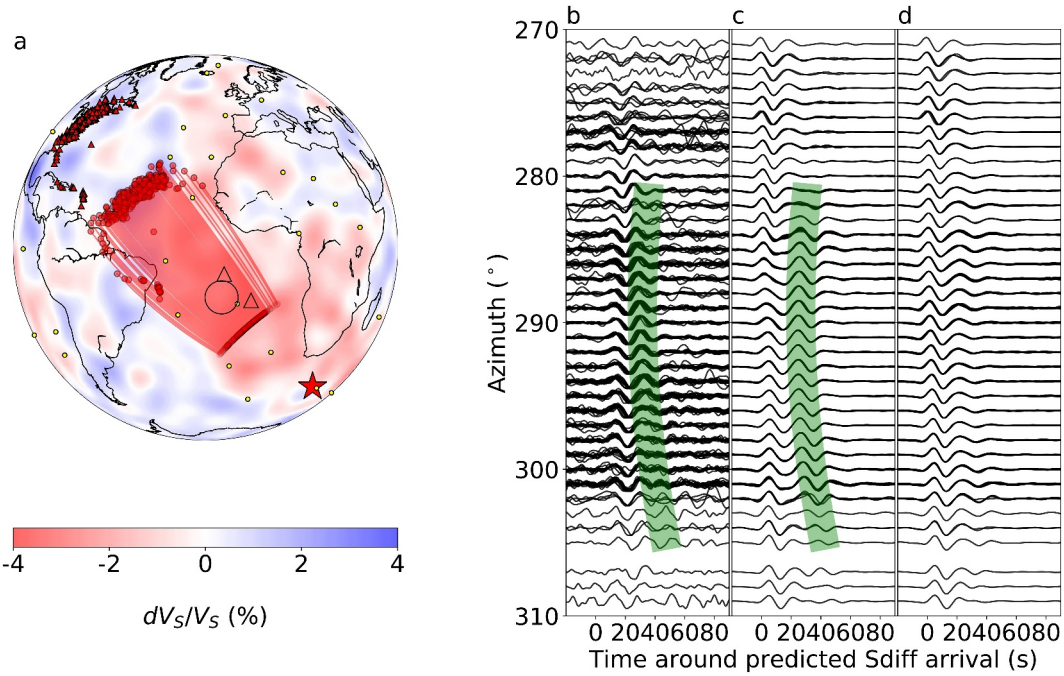

Figure 3. Map and waveforms for event A. (a) Map showing ray paths and proposed ULVZ location. Background velocity model is a depth slice through SEMUCB-WM1 (S. French & Romanowicz, 2014) at 2,800 km depth. (b) Observed data with interpreted postcursors highlighted in green. (c) Synthetics including the proposed ULVZ model within SEMUCB-WM1. Same highlight is shown as in (b) shifted by −5 s (as our S_{diff} waves arrive earlier in the synthetics, see text for discussion). (d) Synthetics for SEMUCB-WM1.

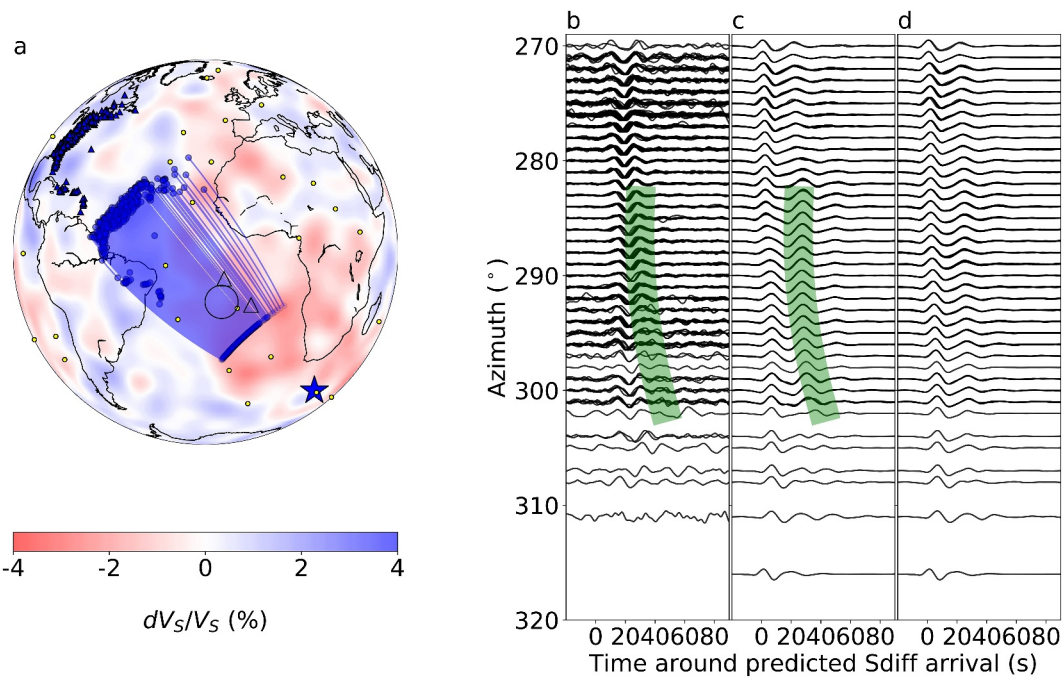

Figure 4. Map and waveforms for event B. (a) Map showing ray paths and proposed ULVZ location. Background velocity model is a depth slice through SEMUCB-WM1 at 2,800 km depth. (b) Observed data with interpreted postcursors highlighted in green. (c) Synthetics including the proposed ULVZ model within SEMUCB-WM1. Same highlight is shown as in (b) shifted by −5 s. (d) Synthetics for SEMUCB-WM1.

15252027, 2024, 7, Downloaded from https://agupubs.onlinelibrary.wiley.com/doi/10.1029/2024GC011559 by Washington University School Of Medicine, Wiley Online Library on [02/05/2025]. See the Terms and Conditions (https://onlinelibrary.wiley.com/terms-and-conditions) on Wiley Online Library for rules of use; OA articles are governed by the applicable Creative Commons License

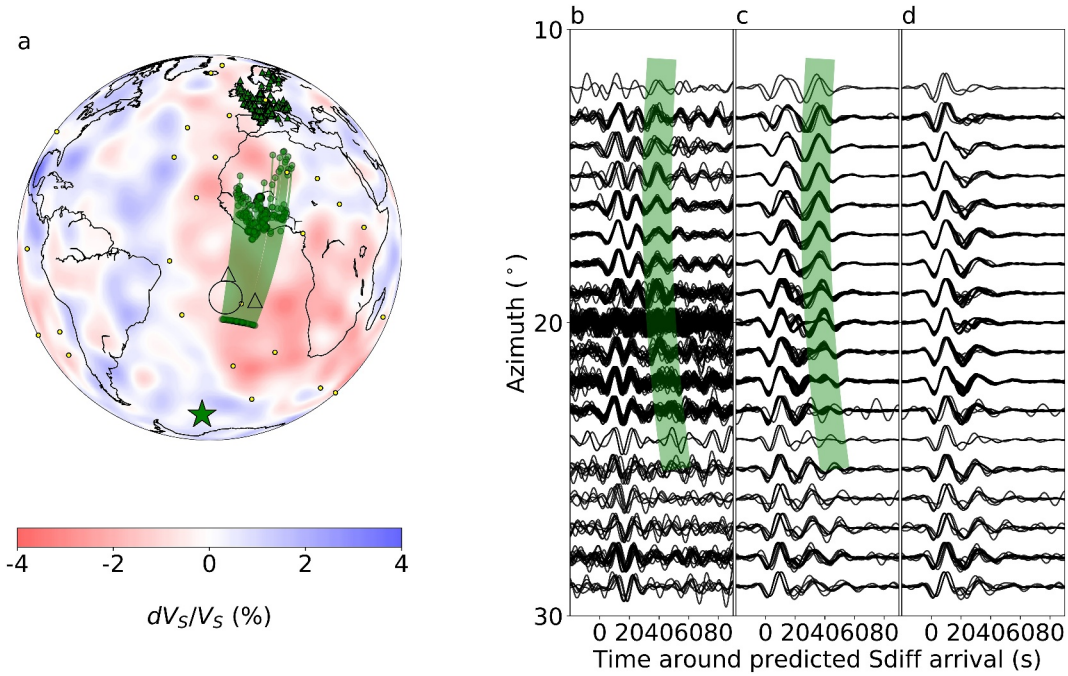

Figure 5. Map and waveforms for event C. (a) Map showing ray paths and proposed ULVZ location. Background velocity model is a depth slice through SEMUCB-WM1 at 2,800 km depth. (b) Observed data with interpreted postcursors highlighted in green. (c) Synthetics including the proposed ULVZ model within SEMUCB-WM1. Same highlight is shown as in (b) shifted by −5 s. (d) Synthetics for SEMUCB-WM1.

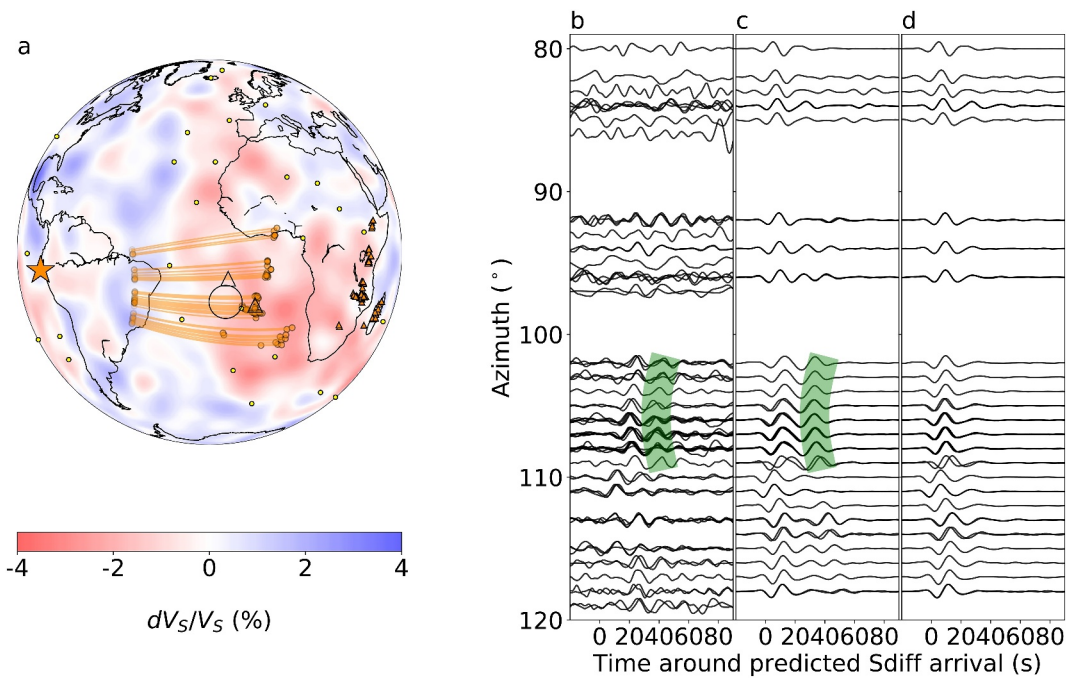

Figure 6. Map and waveforms for event D. (a) Map showing ray paths and proposed ULVZ location. Background velocity model is a depth slice through SEMUCB-WM1 at 2,800 km depth. (b) Observed data with interpreted postcursors highlighted in green. (c) Synthetics including the proposed ULVZ model within SEMUCB-WM1. Same highlight is shown as in (b) shifted by −5 s. (d) Synthetics for SEMUCB-WM1.

15252027, 2024, 7, Downloaded from https://agupubs.onlinelibrary.wiley.com/doi/10.1029/2024GC011559 by Washington University School Of Medicine, Wiley Online Library on [02/05/2025]. See the Terms and Conditions (https://onlinelibrary.wiley.com/terms-and-conditions) on Wiley Online Library for rules of use; OA articles are governed by the applicable Creative Commons License

15252027, 2024, 7, Downloaded from https://agupubs.onlinelibrary.wiley.com/doi/10.1029/2024GC011559 by Washington University School Of Medicine, Wiley Online Library on [02/05/2025]. See the Terms and Conditions (https://onlinelibrary.wiley.com/terms-and-conditions) on Wiley Online Library for rules of use; OA articles are governed by the applicable Creative Commons License

with delay times, relative peak amplitudes, or even presence of postcursor being affected. As those differences are clearly distinguishable, we estimate the uncertainties on each quantity to be half of those amounts.

Across all events, the main S_{diff} phases in the data arrive much later than in the synthetics. The S_{diff} phases in the various orientations all travel through the African LLSVP. The delays caused by this anomaly are likely underestimated by our model as—using the sandwiched-CSEM—we can only include a 3D model in the lowermost 300 km of the mantle, while particularly the African LLSVP can extend much higher (Cottaar & Lekic, 2016). To allow for comparison of move-out patterns, delay times, and relative amplitudes of postcursors, the highlight for the interpreted postcursor is shifted 5 s earlier in the synthetics.

Individual traces are normalized, allowing for comparison for relative amplitudes instead of absolute amplitudes. Generally, the relative amplitude of the postcursor with respect to the main phase is well predicted. The relative delay time between the postcursor and main phase is well fit in events C and D, and slightly large for events A and B.

Waveform results comparing predictions for our preferred model to the observations for three further events are shown in Supporting Information S1 as events S1 to S3. One of these complements what we see for event C here. The second shows an example from a new geometry where strong postcursors should be expected, but are not clearly observed. This could be due to the noisy data, but might also indicated there is some unmodelled asymmetry to the ULVZ's shape. The third is a lower quality event that is co-located with event D.

4. Discussion

4.1. Limitations in Parameterization

Our model does not fit all four events equally well. Likely there are lateral variations and asymmetries in the actual ULVZ that could account for some of the variations, but it is difficult and computationally intensive to assess more parameters in our forward modeling approach. For the Hawaiian ULVZ, the potential of a Bayesian inversion for an elliptical shape has been demonstrated, for which the results showed alignment along the LLSVP boundary (Martin et al., 2023a, 2023b). This approach requires careful picking of the postcursor travel time delays, which is challenging to do for the generally sparser and lower quality data we have here.

While the exact location is uncertain up to several degrees, the good azimuthal coverage does limit where the ULVZ could be. The ULVZ is constrained to lie beneath the vicinity of the St. Helena and Ascension hotspot locations.

4.2. Comparison to Other ULVZs

The discovered "Atlantic" ULVZ lies on the core-mantle boundary to the west of the St. Helena hotspot and to the south of Ascension. No previous studies with other seismic probes suggest evidence of a ULVZ in this region (see compilation in Yu and Garnero (2018)). Global compilations of SPdKS data have too little coverage in this area to observe a ULVZ (Thorne et al., 2021). Ni and Helmberger (2001a) show some evidence of patchy ULVZ material further to the West. Generally, there have been few studies finding ULVZs beneath the Atlantic.

Our modeled Atlantic ULVZ is of comparable size to "mega-ULVZs" in the literature that have been located near major hotspots (e.g., Cottaar & Romanowicz, 2012; Cottaar et al., 2022; Jenkins et al., 2021; Krier et al., 2021; Lai et al., 2022; J. Li et al., 2022; Yuan & Romanowicz, 2017). All of these, like our modeled ULVZ, are located within LLSVPs, or near their edge. The Atlantic ULVZ is the second ULVZ, after the one beneath Iceland that can be linked to the African LLSVP.

While we have modeled its geometry as cylindrical to make synthetic modeling tractable, investigations for ScS pre- and postcursors for Hawaii have shown the mega-ULVZ there has varied morphology (Jenkins et al., 2021). Such modeling requires shorter distance event-station geometry, for which the bounce point samples the ULVZ. Applying this to the Atlantic ULVZ would require new networks of land-based and ocean-bottom seismometers. Data for the Hawaiian ULVZ has also shown internal layering (Z. Li et al., 2022), but such analyses would require higher quality data than is presently available.

Our observations do not provide a direct constraint on the density of the ULVZ. However, the estimated aspect ratio of the ULVZ of 600 km wide and 20 km tall means the density contrast must be large (Bower et al., 2011).

15252027, 2024, 7, Downloaded from https://agupubs.onlinelibrary.wiley.com/doi/10.1029/2024GC011559 by Washington University School Of Medicine, Wiley Online Library on [02/05/2025]. See the Terms and Conditions (https://onlinelibrary.wiley.com/terms-and-conditions) on Wiley Online Library for rules of use; OA articles are governed by the applicable Creative Commons License

Such broad-scale features have been recreated in 3D geodynamical models by including "ultradense" material (M. Li et al., 2017). The observed morphology does not result if ULVZ material is caused purely by partial melting (Dannberg et al., 2021), but partial melting could occur within an already compositionally distinct material.

4.3. Potential Links to Hotspot Locations

Whether (mega-)ULVZs are linked to and play a role in mantle plume dynamics remains speculative. Mega-ULVZs are detected beneath the major hotspots, Hawaii, Iceland, Samoa, and Galápagos, where large buoyancy fluxes are observed (Hoggard et al., 2020) and whole mantle plumes have been imaged (e.g., S. W. French & Romanowicz, 2015). Additionally, basalts from these hotspots exhibit high $^{3}He/^{4}He$ isotope ratios, solar-like neon isotopes, and negative deviations in tungsten isotope ratios that have been suggested to reflect a combination of ULVZ and LLSVP signatures (Cottaar et al., 2022; Mundl-Petermeier et al., 2020). However, a recent study also shows that the Marquesas shows high $^{3}He/^{4}He$ isotope ratios, but no deviation in tungsten isotope ratios (Herret et al., 2023), even though there is suggested to be a ULVZ at its base (Kim et al., 2020).

St. Helena and Ascension are hotspot locations with a weak buoyancy flux (Hoggard et al., 2020). The shear wave tomographic model of S. W. French and Romanowicz (2015) observes a whole mantle plume beneath St. Helena. Based on this model, Bao et al. (2022) categorize St. Helena as a "warm," but not a "hot" plume, and Ascension as a "cold" plume, suggesting the latter might not have a deep-seated source. However, based on a range of tomographic models, Marignier et al. (2020) conclude a higher possibility of a deep-seated plume beneath Ascension than for St. Helena. The nature of the plumes, if both hotspots are fed by a common plume source, and where the plume(s) interact with the African LLSVP and the core-mantle boundary remains uncertain.

St. Helena is geochemically categorized as a HIMU hotspot ("high μ," where μ is the $^{238}U/^{204}Pb$ ratio of the mantle source). Radioactive ^{238}U decays to produce ^{206}Pb over time. Basalts from St. Helena and other HIMU ocean islands, such the Cook-Austral Islands and the Canary Islands, exhibit extremely radiogenic Pb isotopic signatures (high ratios of radiogenic ^{206}Pb to non-radiogenic ^{204}Pb) that require evolution of a source with high U/Pb (high μ) for ∼1.5–2 Gyr timescales (Chauvel et al., 1992; Zindler & Hart, 1986). The HIMU Pb isotopic signature is attributed to ancient recycled oceanic crust in the mantle source, as slab processing during seafloor alteration and dehydration upon subduction generates high U/Pb in the crust (Kelley et al., 2005); this interpretation is supported by various stable isotope ratios (Bai et al., 2022; Blusztajn et al., 2018; Chan et al., 2009; X.-Y. Zhang et al., 2022), though alternate hypotheses have been put forth (see review in Weis et al. (2023)). Nearly all hotspots, including St. Helena, have also been suggested to be basalt-enriched based on the presence of the seismically observable "X discontinuity" around 300 km depth (Kemp et al., 2019; Pugh et al., 2021).

Ancient dehydrated recycled oceanic crust should have extremely radiogenic He isotopes. Crust is thoroughly degassed of He, and mainly ^{4}He is produced over time by alpha decay of U and Th. After 2 billion years of residence in the mantle, recycled crust is expected to develop a $^{3}He/^{4}He$ of ∼0.01 Ra (where Ra is the atmospheric ratio of 1.39×10^{-6}) (Barfod et al., 1999). However, HIMU He isotope ratios range from ∼4–7 Ra (Barfod et al., 1999; Day & Hilton, 2011; Graham et al., 1992; Hanyu & Kaneoka, 1997; Hanyu et al., 2011, 2014; Parai et al., 2009; Sandoval-Velasquez et al., 2023; X. J. Zhang et al., 2024). The observation that HIMU $^{3}He/^{4}He$ ratios (including in samples from St. Helena; Graham et al., 1992; Hanyu et al., 2011) are higher than expected for pure recycled oceanic crust is best explained by mixing between recycled crust and a component with higher $^{3}He/^{4}He$. While HIMU He isotopes could be explained by recycled crust mixing with the mantle source of mid-ocean ridge basalts (MORBs, ∼7–9 Ra), HIMU Ne isotopic data from the Cook-Australs (Parai et al., 2009; X. J. Zhang et al., 2024), Canary Islands (Sandoval-Velasquez et al., 2023) and one Ne measurement from St. Helena (Moreira et al., 2003) are more primitive in character (i.e., come from a less-outgassed reservoir) than the MORB mantle. He-Ne isotope systematics require that HIMU plumes contain a mixture of recycled crust and a high $^{3}He/^{4}He$ component similar to that observed in Hawaii, Iceland, Galapagos, or Samoa (X. J. Zhang et al., 2024).

Ascension is characterized by moderate HIMU Pb and He isotopic signatures, and has been suggested to sample the same source as St. Helena (Ammon et al., 2009). Ne isotopes measured in basalts from Mid-Atlantic Ridge off-axis seamounts near Ascension are similar to the other HIMU Ne observations and require sampling of a component that is less outgassed than the MORB mantle (Stroncik et al., 2007). This could potentially indicate sampling of a deep reservoir, although some debate remains if the mantle plume feeds into this area (Stroncik & Niedermann, 2016).

15252027, 2024, 7, Downloaded from https://agupubs.onlinelibrary.wiley.com/doi/10.1029/2024GC011559 by Washington University School Of Medicine, Wiley Online Library on [02/05/2025]. See the Terms and Conditions (https://onlinelibrary.wiley.com/terms-and-conditions) on Wiley Online Library for rules of use; OA articles are governed by the applicable Creative Commons License

The relatively low St. Helena and Ascension $^{3}He/^{4}He$ ratios compared to other hotspots associated with mega-ULVZs may reflect masking of a high $^{3}He/^{4}He$ signature by mixing with recycled crust rich in ^{4}He. Ne isotopes are not masked in this way. While further Ne isotopic data from St. Helena are desirable, the existing Ne data from the region indicate a contribution from a less-outgassed reservoir. The question remains then whether the LLSVPs or mega-ULVZs are the source of the less-outgassed, high $^{3}He/^{4}He$ and primitive Ne isotopic compositions globally. The anomalous tungsten signatures could be explained by a primordial or core-derived signature that is more easily attributed to the more iron-rich mega-ULVZs (Cottaar et al., 2022; Mundl-Petermeier et al., 2020). Tungsten isotopic data for St. Helena or Ascension would enable further testing of the hypothesis that anomalous tungsten isotopic signatures are found at hotspots associated with mega-ULVZs.

5. Conclusions

We discovered an ultra-low velocity zone beneath the Atlantic Ocean through S_{diff} postcursors and have developed an approximate model which reproduces the S_{diff} postcursors seen in real data, as well as the directionality of scattered energy. From comparison of real and synthetic waveforms, beamforming, and frequency analysis, we constrain our model to a cylinder 600 ± 150 km across, 20 ± 5 km high, and with 30% ± 5% V_S reduction, at 15 ± 2°S, 15 ± 2°W. The intensity of postcursory and scattered energy may imply that the true ULVZ is non-axisymmetric. Unlike other ocean islands above modeled mega-ULVZs such as Hawaii, Iceland, Samoa and Galápagos, St. Helena and Ascension's geochemical signatures reflect sampling of a HIMU reservoir. A geochemical signature from the LLSVP and/or ULVZ could be present, but would need further characterization.

Data Availability Statement

Data were acquired using IRIS Data Services. Data used for events A and B are from the arrays TA (IRIS Transportable Array, 2003), X8 (Menke et al., 2012), LD (Lamont Doherty Earth Observatory (LDEO), Columbia University, 1970), US (Albuquerque Seismological Laboratory (ASL)/USGS, 1990), NE (Albuquerque Seismological Laboratory (ASL)/USGS, 1994), CN (Natural Resources Canada, 1975), N4 (Albuquerque Seismological Laboratory/USGS, 2013), CU (Albuquerque Seismological Laboratory (ASL)/USGS, 2006), 7A (Long & Wiita, 2013), G (Institut de physique du globe de Paris (IPGP) & École et Observatoire des Sciences de la Terre de Strasbourg (EOST), 1982), ZL (Langston et al., 2011), IU (Albuquerque Seismological Laboratory/USGS, 2014), Y6 (Imperial College London, 2013), WI (Institut De Physique Du Globe De Paris (IPGP), 2008), ZC (Pulliam, 2013), PO (Geological Survey of Canada, 2000), XO (Pavlis & Gilbert, 2011), PE (Penn State University, 2004b), CO (University of South Carolina, 1987), GL (Institut De Physique Du Globe De Paris (IPGP), 2020a), TR (University of the West Indies, 1965), YO (Gaherty, 2014), PR (University of Puerto Rico, 1986), MQ (Institut De Physique Du Globe De Paris (IPGP), 2020b), WU (Nanometrics Seismological Instruments, 1991), XQ (Wagner, 2012), Z9 (Fischer et al., 2010), ZU (University of Southampton, 2013), II (Scripps Institution of Oceanography, 1986), ET (University of Memphis, 1982), and DR (National Seismological Centre, 1998). Data used for event C are from the arrays NL (KNMI, 1993), GB (British Geological Survey, 1970), CZ (Charles University in Prague (Czech) et al., 1973), SL (Slovenian Environment Agency, 1990), UP (Swedish National Seismic Network, 1904), FR (RESIF, 1995), CH (Swiss Seismological Service (SED) At ETH Zurich, 1983), HE (Institute Of Seismology, 1980), RD (RESIF, 2018), LX (Instituto Dom Luiz—Faculdade de Ciências da Universidade de Lisboa, 2003), OX (Istituto Nazionale di Oceanografia e di Geofisica Sperimentale—OGS, 2016), OE (ZAMG—Zentralanstalt für Meterologie und Geodynamik, 1987), MN (MedNet Project Partner Institutions, 1990), HU (Kövesligethy Radó Seismological Observatory (Geodetic And Geophysical Institute, Research Centre For Astronomy And Earth Sciences, Hungarian Academy Of Sciences (MTA CSFK GGI KRSZO)), 1992), IM (Various Institutions, 1965), DK (GEUS Geological Survey of Denmark and Greenland, 1976), IU (Albuquerque Seismological Laboratory/USGS, 2014), GR (Federal Institute for Geosciences and Natural Resources, 1976), SK (ESI SAS; Former GPI SAS (Geophysical Institute Of The Slovak Academy Of Sciences), 2004), CA (Institut Cartogràfic i Geològic de Catalunya, 1984), G (Institut de physique du globe de Paris (IPGP) & École et Observatoire des Sciences de la Terre de Strasbourg (EOST), 1982), II (Scripps Institution of Oceanography, 1986), EE (Geological Survey of Estonia (GSE), 1998), SS (Incorporated Research Institutions For Seismology, 1970), MT (French Landslide Observatory—Seismological Datacenter/RESIF, 2006), FN (Sodankyla Geophysical Observatory/University of Oulu, 2005),

LC (Laboratorio Subterraneo de Canfranc, 2011), GE (GEOFON Data Centre, 1993), BE (Royal Observatory of Belgium, 1985), KO (Kandilli Observatory And Earthquake Research Institute, Boğaziçi University, 1971), Z3 (AlpArray Seismic Network, 2015), CL (Corinth Rift Laboratory Team And RESIF Datacenter, 2013), HT (Aristotle University of Thessaloniki, 1981), HL (National Observatory of Athens, Institute of Geodynamics, Athens, 1975), HC (Technological Educational Institute of Crete, 2006), WM (San Fernando Royal Naval Observatory (ROA) et al., 1996), HP (University of Patras, 2000), YW (Guéguen et al., 2017), RO (National Institute for Earth Physics (NIEP Romania), 1994), HA (University of Athens, 2008), MP (Seismological Laboratory of University of Basrah, 2014), and TU (Disaster and Emergency Management Authority, 1990). Data used for event D are from the arrays XK (Gao et al., 2012), IU (Albuquerque Seismological Laboratory/USGS, 2014), NJ (Centre for Geodesy and Geodynamics, 2009), YQ (Gaherty et al., 2013), XM (The ARGOS Project, 2012), XV (Wysession et al., 2011), GE (GEOFON Data Centre, 1993), 1C (Velasco et al., 2011), AF (Penn State University, 2004a), XJ (Ebinger, 2013), and YV (Barruol et al., 2017). Data were processed using ObsPy version 1.1.1 (Beyreuther et al., 2010; Krischer et al., 2015). Figures were created using MatPlotLib version 3.6.3 (Hunter, 2007).

Acknowledgments

We would like to thank Jonathan Wolf and a second reviewer for their comments and suggestions which improved our manuscript. We would like to thank Stuart Russell, Florian Millet, Stephen Pugh, and George Pindar for helpful conversations and advice. This project has received funding from the European Research Council (ERC) under the European Union's Horizon 2020 research and innovation programme (Grant agreement No. 804071 -ZoomDeep). RP was supported by National Science Foundation Grant EAR 2145663. This work was performed using resources provided by the Cambridge Service for Data Driven Discovery (CSD3) operated by the University of Cambridge Research Computing Service (www.csd3.cam.ac.uk), provided by Dell EMC and Intel using Tier-2 funding from the Engineering and Physical Sciences Research Council (capital Grant EP/T022159/1), and DiRAC funding from the Science and Technology Facilities Council (www.dirac.ac.uk). The facilities of IRIS Data Services, and specifically the IRIS Data Management Center, were used for access to waveforms and related metadata used in this study. IRIS Data Services are funded through the Seismological Facilities for the Advancement of Geoscience (SAGE) Award of the National Science Foundation under Cooperative Support Agreement EAR-1851048.

References

Albuquerque Seismological Laboratory (ASL)/USGS. (1990). United States national seismic network [Dataset]. *International Federation of Digital Seismograph Networks*. https://doi.org/10.7914/SN/US

Albuquerque Seismological Laboratory (ASL)/USGS. (1994). New England seismic network [Dataset]. *International Federation of Digital Seismograph Networks*. https://doi.org/10.7914/SN/NE

Albuquerque Seismological Laboratory (ASL)/USGS. (2006). Caribbean network [Dataset]. *International Federation of Digital Seismograph Networks*. https://doi.org/10.7914/SN/CU

Albuquerque Seismological Laboratory/USGS. (2013). Central and eastern US network [Dataset]. *International Federation of Digital Seismograph Networks*. https://doi.org/10.7914/SN/N4

Albuquerque Seismological Laboratory/USGS. (2014). Global seismograph network (GSN—IRIS/USGS) [Dataset]. *International Federation of Digital Seismograph Networks*. https://doi.org/10.7914/SN/IU

AlpArray Seismic Network. (2015). Alparray seismic network (AASN) temporary component [Dataset]. *AlpArray Working Group*. https://doi.org/10.12686/ALPARRAY/Z3_2015

Ammon, K., Dunai, T., Stuart, F., Meriaux, A.-S., & Gayer, E. (2009). Cosmogenic ^{3}He exposure ages and geochemistry of basalts from Ascension Island, Atlantic Ocean. *Quaternary Geochronology*, *4*(6), 525–532. https://doi.org/10.1016/j.quageo.2009.09.003

Aristotle University of Thessaloniki. (1981). Aristotle University of Thessaloniki seismological network [Dataset]. *International Federation of Digital Seismograph Networks*. https://doi.org/10.7914/SN/HT

Bai, R., Jackson, M. G., Huang, F., Moynier, F., Devos, G., Halldórsson, S. A., et al. (2022). Barium isotopes in ocean island basalts as tracers of mantle processes. *Geochimica et Cosmochimica Acta*, *336*, 436–447. https://doi.org/10.1016/j.gca.2022.08.023

Bao, X., Lithgow-Bertelloni, C. R., Jackson, M. G., & Romanowicz, B. (2022). On the relative temperatures of Earth's volcanic hotspots and mid-ocean ridges. *Science*, *375*(6576), 57–61. https://doi.org/10.1126/science.abj8944

Barfod, D. N., Ballentine, C. J., Halliday, A. N., & Fitton, J. G. (1999). Noble gases in the Cameroon line and the He, Ne, and Ar isotopic compositions of high μ (HIMU) mantle. *Journal of Geophysical Research*, *104*(B12), 29509–29527. https://doi.org/10.1029/1999JB900280

Barruol, G., & Sigloch, K., & RHUM-RUM Group, & RESIF. (2017). Rhum-rum experiment, 2011-2015, code YV (réunion hotspot and upper mantle—réunion's unterer mantel) funded by ANR, DFG, CNRS-INSU, IPEV, TAAF, instrumented by DEPAS, INSU-OBS, AWI and the Universities of Muenster, Bonn, La Réunion [Dataset]. *RESIF—Réseau Sismologique et géodésique Français*. https://doi.org/10.15778/RESIF.YV2011

Beyreuther, M., Barsch, R., Krischer, L., Megies, T., Behr, Y., & Wassermann, J. (2010). ObsPy: A python toolbox for seismology. *Seismological Research Letters*, *81*(3), 530–533. https://doi.org/10.1785/gssrl.81.3.530

Blusztajn, J., Nielsen, S. G., Marschall, H. R., Shu, Y., Ostrander, C. M., & Hanyu, T. (2018). Thallium isotope systematics in volcanic rocks from St. Helena–constraints on the origin of the HIMU reservoir. *Chemical Geology*, *476*, 292–301. https://doi.org/10.1016/j.chemgeo.2017.11.025

Bower, D. J., Wicks, J. K., Gurnis, M., & Jackson, J. M. (2011). A geodynamic and mineral physics model of a solid-state ultralow-velocity zone. *Earth and Planetary Science Letters*, *303*(3–4), 193–202. https://doi.org/10.1016/j.epsl.2010.12.035

British Geological Survey. (1970). Great Britain seismograph network [Dataset]. *International Federation of Digital Seismograph Networks*. https://doi.org/10.7914/AV8J-NC83

Capdeville, Y., Chaljub, E., & Montagner, J. P. (2003). Coupling the spectral element method with a modal solution for elastic wave propagation in global Earth models. *Geophysical Journal International*, *152*(1), 34–67. https://doi.org/10.1046/j.1365-246X.2003.01808.x

Centre for Geodesy and Geodynamics. (2009). Nigerian national network of seismographi stations (NNNSS) [Dataset]. *International Federation of Digital Seismograph Networks*. https://doi.org/10.7914/SN/NJ

Chan, L.-H., Lassiter, J. C., Hauri, E. H., Hart, S. R., & Blusztajn, J. (2009). Lithium isotope systematics of lavas from the Cook–Austral islands: Constraints on the origin of HIMU mantle. *Earth and Planetary Science Letters*, *277*(3–4), 433–442. https://doi.org/10.1016/j.epsl.2008.11.009

Charles University in Prague (Czech), Institute of Geonics, Institute of Geophysics, Academy of Sciences of the Czech Republic, Institute of Physics of the Earth Masaryk University (Czech), & Institute of Rock Structure and Mechanics. (1973). Czech regional seismic network [Dataset]. *International Federation of Digital Seismograph Networks*. https://doi.org/10.7914/SN/CZ

Chauvel, C., Hofmann, A. W., & Vidal, P. (1992). HIMU-EM: Connection. *Earth and Planetary Science Letters*, *110*(1–4), 99–119. https://doi.org/10.1016/0012-821X(92)90042-T

Corinth Rift Laboratory Team And RESIF Datacenter. (2013). CL—Corinth rift laboratory seismological network (CRLNET). [Dataset]. *RESIF—Réseau Sismologique et géodésique Français*. https://doi.org/10.15778/RESIF.CL

Cottaar, S., & Lekic, V. (2016). Morphology of seismically slow lower-mantle structures. *Geophysical Journal International*, *207*(2), 1122–1136. https://doi.org/10.1093/gji/ggw324

15252027, 2024, 7, Downloaded from https://agupubs.onlinelibrary.wiley.com/doi/10.1029/2024GC011559 by Washington University School Of Medicine, Wiley Online Library on [02/05/2025]. See the Terms and Conditions (https://onlinelibrary.wiley.com/terms-and-conditions) on Wiley Online Library for rules of use; OA articles are governed by the applicable Creative Commons License

Cottaar, S., Martin, C., Li, Z., & Parai, R. (2022). The root to the galápagos mantle plume on the core-mantle boundary. *Seismica*, *1*(1). https://doi.org/10.26443/seismica.v1i1.197

Cottaar, S., & Romanowicz, B. (2012). An unusually large ULVZ at the base of the mantle near Hawaii. *Earth and Planetary Science Letters*, *355*, 213–222. https://doi.org/10.1016/j.epsl.2012.09.005

Dannberg, J., Myhill, R., Gassmöller, R., & Cottaar, S. (2021). The morphology, evolution and seismic visibility of partial melt at the core–mantle boundary: Implications for ULVZs. *Geophysical Journal International*, *227*(2), 1028–1059. https://doi.org/10.1093/gji/ggab242

Day, J. M., & Hilton, D. R. (2011). Origin of $^{3}He/^{4}He$ ratios in HIMU-type basalts constrained from Canary Island lavas. *Earth and Planetary Science Letters*, *305*(1–2), 226–234. https://doi.org/10.1016/j.epsl.2011.03.006

Disaster and Emergency Management Authority. (1990). Turkish national seismic network [Dataset]. *Department of Earthquake, Disaster and Emergency Management Authority*. https://doi.org/10.7914/SN/TU

Dobrosavljevic, V. V., Sturhahn, W., & Jackson, J. M. (2019). Evaluating the role of iron-rich (Mg, Fe) O in ultralow velocity zones. *Minerals*, *9*(12), 762. https://doi.org/10.3390/min9120762

Dziewonski, A. M., & Anderson, D. L. (1981). Preliminary reference Earth model. *Physics of the Earth and Planetary Interiors*, *25*(4), 297–356. https://doi.org/10.1016/0031-9201(81)90046-7

Ebinger, C. (2013). Magadi-natron magmatic rifting studies [Dataset]. *International Federation of Digital Seismograph Networks*. https://doi.org/10.7914/SN/XJ_2013

Ekström, G., Nettles, M., & Dziewoński, A. (2012). The global CMT project 2004–2010: Centroid-moment tensors for 13,017 earthquakes. *Physics of the Earth and Planetary Interiors*, *200–201*, 1–9. https://doi.org/10.1016/j.pepi.2012.04.002

ESI SAS; Former GPI SAS (Geophysical Institute Of The Slovak Academy Of Sciences). (2004). National network of seismic stations of Slovakia [Dataset]. *GFZ Data Services*. https://doi.org/10.14470/FX099882

Federal Institute for Geosciences and Natural Resources. (1976). German regional seismic network (GRSN) [Dataset]. *Bundesanstalt für Geowissenschaften und Rohstoffe*. https://doi.org/10.25928/MBX6-HR74

Fischer, K. M., Hawman, R. B., & Wagner, L. S. (2010). Southeastern suture of the Appalachian margin experiment. [Dataset]. *International Federation of Digital Seismograph Networks*. https://doi.org/10.7914/SN/Z9_2010

French, S., & Romanowicz, B. A. (2014). Whole-mantle radially anisotropic shear velocity structure from spectral-element waveform tomography. *Geophysical Journal International*, *199*(3), 1303–1327. https://doi.org/10.1093/gji/ggu334

French, S. W., & Romanowicz, B. (2015). Broad plumes rooted at the base of the Earth's mantle beneath major hotspots. *Nature*, *525*(7567), 95–99. https://doi.org/10.1038/nature14876

French Landslide Observatory—Seismological Datacenter/RESIF. (2006). Observatoire multi-disciplinaire des instabilités de versants (OMIV) [Dataset]. *RESIF—Réseau Sismologique et géodésique Français*. https://doi.org/10.15778/RESIF.MT

Gaherty, J. (2014). Eastern North American margin community seismic experiment [Dataset]. *International Federation of Digital Seismograph Networks*. https://doi.org/10.7914/SN/YO_2014

Gaherty, J., Ebinger, C., Nyblade, A., & Shillington, D. (2013). Study of extension and magmatism in Malawi and Tanzania [Dataset]. *International Federation of Digital Seismograph Networks*. https://doi.org/10.7914/SN/YQ_2013

Gao, S., Liu, K., Abdelsalam, M., & Hogan, J. (2012). Seismic arrays for African rift initiation [Dataset]. *International Federation of Digital Seismograph Networks*. https://doi.org/10.7914/SN/XK_2012

GEOFON Data Centre. (1993). GEOFON seismic network [Dataset]. *Deutsches GeoForschungsZentrum GFZ*. https://doi.org/10.14470/TR560404

Geological Survey of Canada. (2000). Portable observatories for lithospheric analysis and research investigating seismicity (Polaris) [Dataset]. *International Federation of Digital Seismograph Networks*. Retrieved from http://www.fdsn.org/networks/detail/PO/

Geological Survey of Estonia (GSE). (1998). Estonian seismic network [Dataset]. *International Federation of Digital Seismograph Networks*. Retrieved from http://www.fdsn.org/networks/detail/EE/

GEUS Geological Survey of Denmark and Greenland. (1976). Danish seismological network [Dataset]. *International Federation of Digital Seismograph Networks*. Retrieved from http://www.fdsn.org/networks/detail/DK/

Graham, D. W., Humphris, S. E., Jenkins, W. J., & Kurz, M. D. (1992). Helium isotope geochemistry of some volcanic rocks from Saint Helena. *Earth and Planetary Science Letters*, *110*(1–4), 121–131. https://doi.org/10.1016/0012-821X(92)90043-U

Guéguen, P., Coutant, O., & Langlais, M., & RESIF. (2017). Maurienne seismic swarm 2017-2018 [Dataset]. *RESIF—Réseau Sismologique et géodésique Français*. https://doi.org/10.15778/RESIF.YW2017

Hanyu, T., & Kaneoka, I. (1997). The uniform and low $^{3}He/^{4}He$ ratios of HIMU basalts as evidence for their origin as recycled materials. *Nature*, *390*(6657), 273–276. https://doi.org/10.1038/36835

Hanyu, T., Kawabata, H., Tatsumi, Y., Kimura, J.-I., Hyodo, H., Sato, K., et al. (2014). Isotope evolution in the HIMU reservoir beneath St. Helena: Implications for the mantle recycling of U and Th. *Geochimica et Cosmochimica Acta*, *143*, 232–252. https://doi.org/10.1016/j.gca.2014.03.016

Hanyu, T., Tatsumi, Y., & Kimura, J.-I. (2011). Constraints on the origin of the HIMU reservoir from He–Ne–Ar isotope systematics. *Earth and Planetary Science Letters*, *307*(3–4), 377–386. https://doi.org/10.1016/j.epsl.2011.05.012

Helmberger, D., Ni, S., Wen, L., & Ritsema, J. (2000). Seismic evidence for ultralow-velocity zones beneath Africa and eastern Atlantic. *Journal of Geophysical Research*, *105*(B10), 23865–23878. https://doi.org/10.1029/2000JB900143

Herret, M.-T., Peters, B., Kim, D., Castillo, P., & Mundl-Petermeier, A. (2023). Decoupling of short-lived radiogenic and helium isotopes in the Marquesas hotspot. *Chemical Geology*, *640*, 121727. https://doi.org/10.1016/j.chemgeo.2023.121727

Hoggard, M. J., Parnell-Turner, R., & White, N. (2020). Hotspots and mantle plumes revisited: Towards reconciling the mantle heat transfer discrepancy. *Earth and Planetary Science Letters*, *542*, 116317. https://doi.org/10.1016/j.epsl.2020.116317

Hunter, J. D. (2007). Matplotlib: A 2D graphics environment. *Computing in Science & Engineering*, *9*(03), 90–95. https://doi.org/10.1109/mcse.2007.55

Imperial College London. (2013). Network QM-III-UK [Dataset]. *International Federation of Digital Seismograph Networks*. Retrieved from http://www.fdsn.org/networks/detail/Y6_2013/

Incorporated Research Institutions For Seismology. (1970). Single station [Dataset]. *International Federation of Digital Seismograph Networks*. https://doi.org/10.7914/SN/SS

Institut Cartogràfic i Geològic de Catalunya. (1984). Catalan seismic network [Dataset]. *International Federation of Digital Seismograph Networks*. https://doi.org/10.7914/SN/CA

Institut De Physique Du Globe De Paris (IPGP). (2008). GNSS, seismic broadband and strong motion permanent networks in West Indies [Dataset]. *Institut de physique du globe de Paris (IPGP), Université de Paris*. https://doi.org/10.18715/ANTILLES.WI

15252027, 2024, 7, Downloaded from https://agupubs.onlinelibrary.wiley.com/doi/10.1029/2024GC011559 by Washington University School Of Medicine, Wiley Online Library on [02/05/2025]. See the Terms and Conditions (https://onlinelibrary.wiley.com/terms-and-conditions) on Wiley Online Library for rules of use; OA articles are governed by the applicable Creative Commons License

Institut De Physique Du Globe De Paris (IPGP). (2020a). Seismic, tiltmeter, extensometer, tide, magnetic and weather permanent networks on la Soufrière volcano and Guadeloupe [Dataset]. *Institut de physique du globe de Paris (IPGP), Université de Paris*. https://doi.org/10.18715/GUADELOUPE.GL

Institut De Physique Du Globe De Paris (IPGP). (2020b). Seismic, tiltmeter, groundwater, magnetic and weather permanent networks on Montagne Pelée volcano and Martinique [Dataset]. *Institut de physique du globe de Paris (IPGP), Université de Paris*. https://doi.org/10.18715/MARTINIQUE.MQ

Institut de physique du globe de Paris (IPGP), & École et Observatoire des Sciences de la Terre de Strasbourg (EOST). (1982). Geoscope, French global network of broad band seismic stations [Dataset]. *Institut de physique du globe de Paris (IPGP), Université de Paris*. https://doi.org/10.18715/GEOSCOPE.G

Institute Of Seismology, U. O. H. (1980). The Finnish national seismic network [Dataset]. *GFZ Data Services*. https://doi.org/10.14470/UR044600

Instituto Dom Luiz—Faculdade de Ciências da Universidade de Lisboa. (2003). Instituto dom luiz (idl)—faculdade de ciencias universidade de lisboa [Dataset]. *International Federation of Digital Seismograph Networks*. https://doi.org/10.7914/SN/LX

IRIS Transportable Array. (2003). Usarray transportable array [Dataset]. *International Federation of Digital Seismograph Networks*. https://doi.org/10.7914/SN/TA

Istituto Nazionale di Oceanografia e di Geofisica Sperimentale—OGS. (2016). North-East Italy seismic network [Dataset]. *FDSN*. https://doi.org/10.7914/SN/OX

Jackson, M. G., Konter, J. G., & Becker, T. (2017). Primordial helium entrained by the hottest mantle plumes. *Nature*, *542*(7641), 340–343. https://doi.org/10.1038/nature21023

Jenkins, J., Mousavi, S., Li, Z., & Cottaar, S. (2021). A high-resolution map of Hawaiian ULVZ morphology from ScS phases. *Earth and Planetary Science Letters*, *563*, 116885. https://doi.org/10.1016/j.epsl.2021.116885

Kandilli Observatory And Earthquake Research Institute, Boğaziçi University. (1971). Kandilli observatory and earthquake research institute (KOERI) [Dataset]. *International Federation of Digital Seismograph Networks*. https://doi.org/10.7914/SN/KO

Kelley, K. A., Plank, T., Farr, L., Ludden, J., & Staudigel, H. (2005). Subduction cycling of U, Th, and Pb. *Earth and Planetary Science Letters*, *234*(3–4), 369–383. https://doi.org/10.1016/j.epsl.2005.03.005

Kemp, M., Jenkins, J., Maclennan, J., & Cottaar, S. (2019). X-discontinuity and transition zone structure beneath Hawaii suggests a heterogeneous plume. *Earth and Planetary Science Letters*, *527*, 115781. https://doi.org/10.1016/j.epsl.2019.115781

Kim, D., Lekić, V., Ménard, B., Baron, D., & Taghizadeh-Popp, M. (2020). Sequencing seismograms: A panoptic view of scattering in the core-mantle boundary region. *Science*, *368*(6496), 1223–1228. https://doi.org/10.1126/science.aba8972

Kimura, T., Ohfuji, H., Nishi, M., & Irifune, T. (2017). Melting temperatures of MgO under high pressure by micro-texture analysis. *Nature Communications*, *8*(1), 1–7. https://doi.org/10.1038/ncomms15735

KNMI. (1993). Netherlands seismic and acoustic network [Dataset]. *Royal Netherlands Meteorological Institute (KNMI)*. https://doi.org/10.21944/E970FD34-23B9-3411-B366-E4F72877D2C5

Kövesligethy Radó Seismological Observatory (Geodetic And Geophysical Institute, Research Centre For Astronomy And Earth Sciences, Hungarian Academy Of Sciences (MTA CSFK GGI KRSZO)). (1992). Hungarian national seismological network [Dataset]. *GFZ Data Services*. https://doi.org/10.14470/UH028726

Krier, J., Thorne, M. S., Leng, K., & Nissen-Meyer, T. (2021). A compositional component to the Samoa ultralow-velocity zone revealed through 2-and 3-D waveform modeling of SKS and SKKS differential travel-times and amplitudes. *Journal of Geophysical Research: Solid Earth*, *126*(7), e2021JB021897. https://doi.org/10.1029/2021JB021897

Krischer, L., Megies, T., Barsch, R., Beyreuther, M., Lecocq, T., Caudron, C., & Wassermann, J. (2015). ObsPy: A bridge for seismology into the scientific python ecosystem. *Computational Science & Discovery*, *8*(1), 014003. https://doi.org/10.1088/1749-4699/8/1/014003

Laboratorio Subterraneo de Canfranc. (2011). Lsc (laboratorio subterraneo canfranc) [Dataset]. *International Federation of Digital Seismograph Networks*. https://doi.org/10.7914/SN/LC

Lai, V. H., Helmberger, D. V., Dobrosavljevic, V. V., Wu, W., Sun, D., Jackson, J. M., & Gurnis, M. (2022). Strong ULVZ and slab interaction at the northeastern edge of the Pacific LLSVP favors plume generation. *Geochemistry, Geophysics, Geosystems*, *23*(2), e2021GC010020. https://doi.org/10.1029/2021GC010020

Lamont Doherty Earth Observatory (LDEO), Columbia University. (1970). Lamont-Doherty cooperative seismographic network [Dataset]. *International Federation of Digital Seismograph Networks*. https://doi.org/10.7914/SN/LD

Langston, C., DeShon, H., Powell, C., Horton, S., Ammon, C., Herrmann, R., & Thomas, W. (2011). Northern embayment lithospheric experiment [Dataset]. *International Federation of Digital Seismograph Networks*. https://doi.org/10.7914/SN/ZL_2011

Lay, T., Garnero, E. J., & Williams, Q. (2004). Partial melting in a thermo-chemical boundary layer at the base of the mantle. *Physics of the Earth and Planetary Interiors*, *146*(3–4), 441–467. https://doi.org/10.1016/j.pepi.2004.04.004

Li, J., Sun, D., & Bower, D. J. (2022). Slab control on the mega-sized North Pacific ultra-low velocity zone. *Nature Communications*, *13*(1), 1–11. https://doi.org/10.1038/s41467-022-28708-8

Li, M., McNamara, A. K., Garnero, E. J., & Yu, S. (2017). Compositionally-distinct ultra-low velocity zones on Earth's core-mantle boundary. *Nature Communications*, *8*(1), 177. https://doi.org/10.1038/s41467-017-00219-x

Li, Z., Leng, K., Jenkins, J., & Cottaar, S. (2022). Kilometer-scale structure on the core–mantle boundary near Hawaii. *Nature Communications*, *13*(1), 1–8. https://doi.org/10.1038/s41467-022-30502-5

Long, M., & Wiita, P. (2013). Mid-Atlantic geophysical integrative collaboration [Dataset]. *International Federation of Digital Seismograph Networks*. https://doi.org/10.7914/SN/7A_2013

Marignier, A., Ferreira, A. M. G., & Kitching, T. (2020). The probability of mantle plumes in global tomographic models. *Geochemistry, Geophysics, Geosystems*, *21*(9), e2020GC009276. https://doi.org/10.1029/2020GC009276

Martin, C., Bodin, T., & Cottaar, S. (2023a). Mapping structures on the core–mantle boundary using Sdiff postcursors: Part II. Application to the Hawaiian ULVZ. *Geophysical Journal International*, *235*(3), 2399–2409. https://doi.org/10.1093/gji/ggad345

Martin, C., Bodin, T., & Cottaar, S. (2023b). Mapping structures on the core–mantle boundary using Sdiff postcursors: Part I. Method and validation. *Geophysical Journal International*, *235*(3), 2385–2398. https://doi.org/10.1093/gji/ggad340

MedNet Project Partner Institutions. (1990). Mediterranean very broadband seismographic network (MedNet) [Dataset]. *Istituto Nazionale di Geofisica e Vulcanologia (INGV)*. https://doi.org/10.13127/SD/FBBBTDTD6Q

Menke, W., Levin, V., & Darbyshire, F. (2012). Deep structure of three continental sutures in eastern North America [Dataset]. *International Federation of Digital Seismograph Networks*. https://doi.org/10.7914/SN/X8_2012

Moreira, M., Doucet, S., Madureira, P., Lecomte, A., & Allegre, C. (2003). He-Ne systematics in OIB and the nature of the source of mantle plumes. In *AGU fall meeting abstracts* (p. V32A-1007). https://doi.org/10.1016/j.jvolgeores.2023.107928

15252027, 2024, 7, Downloaded from https://agupubs.onlinelibrary.wiley.com/doi/10.1029/2024GC011559 by Washington University School Of Medicine, Wiley Online Library on [02/05/2025]. See the Terms and Conditions (https://onlinelibrary.wiley.com/terms-and-conditions) on Wiley Online Library for rules of use; OA articles are governed by the applicable Creative Commons License

Mundl, A., Touboul, M., Jackson, M. G., Day, J. M., Kurz, M. D., Lekic, V., et al. (2017). Tungsten-182 heterogeneity in modern ocean island basalts. *Science*, *356*(6333), 66–69. https://doi.org/10.1126/science.aal4179

Mundl-Petermeier, A., Walker, R., Fischer, R., Lekic, V., Jackson, M., & Kurz, M. (2020). Anomalous 182W in high $^{3}He/^{4}He$ ocean island basalts: Fingerprints of Earth's core? *Geochimica et Cosmochimica Acta*, *271*, 194–211. https://doi.org/10.1016/j.gca.2019.12.020

Nanometrics Seismological Instruments. (1991). The southern Ontario seismic network (SOSN) [Dataset]. *International Federation of Digital Seismograph Networks*. Retrieved from http://www.fdsn.org/networks/detail/WU/

National Institute for Earth Physics (NIEP Romania). (1994). Romanian seismic network [Dataset]. *International Federation of Digital Seismograph Networks*. https://doi.org/10.7914/SN/RO

National Observatory of Athens, Institute of Geodynamics, Athens. (1975). National observatory of Athens seismic network [Dataset]. *International Federation of Digital Seismograph Networks*. https://doi.org/10.7914/SN/HL

National Seismological Centre. (1998). Centro nacional de sismologia [Dataset]. *International Federation of Digital Seismograph Networks*. https://doi.org/10.7914/SN/DR

Natural Resources Canada. (1975). Canadian national seismograph network [Dataset]. *International Federation of Digital Seismograph Networks*. https://doi.org/10.7914/SN/CN

Ni, S., & Helmberger, D. V. (2001a). Horizontal transition from fast to slow structures at the core–mantle boundary; South Atlantic. *Earth and Planetary Science Letters*, *187*(3), 301–310. https://doi.org/10.1016/S0012-821X(01)00273-4

Ni, S., & Helmberger, D. V. (2001b). Probing an ultra-low velocity zone at the core mantle boundary with P and S waves. *Geophysical Research Letters*, *28*(12), 2345–2348. https://doi.org/10.1029/2000GL012766

Parai, R., Mukhopadhyay, S., & Lassiter, J. C. (2009). New constraints on the HIMU mantle from neon and helium isotopic compositions of basalts from the cook-austral islands. *Earth and Planetary Science Letters*, *277*(1–2), 253–261. (Times Cited: 1). https://doi.org/10.1016/j.epsl.2008.10.014

Pavlis, G., & Gilbert, H. (2011). Ozark Illinois Indiana Kentucky (OIINK) flexible array experiment [Dataset]. *International Federation of Digital Seismograph Networks*. https://doi.org/10.7914/SN/XO_2011

Penn State University. (2004a). Africaarray [Dataset]. *International Federation of Digital Seismograph Networks*. https://doi.org/10.7914/SN/AF

Penn State University. (2004b). Pennsylvania state seismic network [Dataset]. *International Federation of Digital Seismograph Networks*. https://doi.org/10.7914/SN/PE

Pugh, S., Jenkins, J., Boyce, A., & Cottaar, S. (2021). Global receiver function observations of the X-discontinuity reveal recycled basalt beneath hotspots. *Earth and Planetary Science Letters*, *561*, 116813. https://doi.org/10.1016/j.epsl.2021.116813

Pulliam, J. (2013). Greater Antilles seismic program [Dataset]. *International Federation of Digital Seismograph Networks*. https://doi.org/10.7914/SN/ZC_2013

RESIF. (1995). RESIF-RLBP French broad-band network, RESIF-RAP strong motion network and other seismic stations in metropolitan France [Dataset]. *RESIF—Réseau Sismologique et géodésique Français*. https://doi.org/10.15778/RESIF.FR

RESIF. (2018). CEA/DASE broad-band permanent network in metropolitan France [Dataset]. *RESIF—Réseau Sismologique et géodésique Français*. https://doi.org/10.15778/RESIF.RD

Royal Observatory of Belgium. (1985). Belgian seismic network [Dataset]. *International Federation of Digital Seismograph Networks*. https://doi.org/10.7914/SN/BE

Sandoval-Velasquez, A., Rizzo, A., Casetta, F., Ntaflos, T., Aiuppa, A., Alonso, M., et al. (2023). The noble gas signature of the 2021 Tajogaite eruption La Palma, Canary Islands. *Journal of Volcanology and Geothermal Research*, *443*, 107928. https://doi.org/10.1016/j.jvolgeores.2023.107928

San Fernando Royal Naval Observatory (ROA), Universidad Complutense De Madrid (UCM), Helmholtz-Zentrum Potsdam Deutsches GeoForschungsZentrum (GFZ), Universidade De Évora (UEVORA, Portugal), & Institute Scientifique Of Rabat (ISRABAT, Morocco). (1996). The western Mediterranean BB seismic network [Dataset]. *Deutsches GeoForschungsZentrum GFZ*. https://doi.org/10.14470/JZ581150

Scripps Institution of Oceanography. (1986). Global seismograph network—IRIS/IDA [Dataset]. *International Federation of Digital Seismograph Networks*. https://doi.org/10.7914/SN/II

Seismological Laboratory of University of Basrah. (2014). Iraqi seismic observatory [Dataset]. *International Federation of Digital Seismograph Networks*. https://doi.org/10.7914/SN/MP

Slovenian Environment Agency. (1990). Seismic network of the republic of Slovenia [Dataset]. *International Federation of Digital Seismograph Networks*. https://doi.org/10.7914/SN/SL

Sodankyla Geophysical Observatory/University of Oulu. (2005). Northern Finland seismic network [Dataset]. *International Federation of Digital Seismograph Networks*. Retrieved from http://www.fdsn.org/networks/detail/FN/

Stroncik, N. A., & Niedermann, S. (2016). He, Ne and Ar isotope signatures of mid-ocean ridge basalts and their implications for upper mantle structure: A case study from the Mid-Atlantic Ridge at 4–12°S. *Geochimica et Cosmochimica Acta*, *183*, 94–105. https://doi.org/10.1016/j.gca.2016.04.002

Stroncik, N. A., Niedermann, S., & Haase, K. M. (2007). Neon and helium isotopes as tracers of mantle reservoirs and mantle dynamics. *Earth and Planetary Science Letters*, *258*(1), 334–344. https://doi.org/10.1016/j.epsl.2007.03.046

Swedish National Seismic Network. (1904). Swedish national seismic network [Dataset]. *Uppsala University*. https://doi.org/10.18159/SNSN

Swiss Seismological Service (SED) At ETH Zurich. (1983). National seismic networks of Switzerland [Dataset]. *ETH Zürich*. https://doi.org/10.12686/SED/NETWORKS/CH

Technological Educational Institute of Crete. (2006). Seismological network of Crete [Dataset]. *International Federation of Digital Seismograph Networks*. https://doi.org/10.7914/SN/HC

The ARGOS Project. (2012). ARGOS—Alutu and regional geophysical observation study [Dataset]. *International Federation of Digital Seismograph Networks*. https://doi.org/10.7914/SN/XM_2012

Thorne, M. S., Garnero, E. J., Jahnke, G., Igel, H., & McNamara, A. K. (2013). Mega ultra low velocity zone and mantle flow. *Earth and Planetary Science Letters*, *364*, 59–67. https://doi.org/10.1016/j.epsl.2012.12.034

Thorne, M. S., Leng, K., Pachhai, S., Rost, S., Wicks, J., & Nissen-Meyer, T. (2021). The most parsimonious ultralow-velocity zone distribution from highly anomalous SPdKS waveforms. *Geochemistry, Geophysics, Geosystems*, *22*(1), e2020GC009467. https://doi.org/10.1029/2020GC009467

University of Athens. (2008). Hellenic seismological network, University of Athens, seismological laboratory [Dataset]. *International Federation of Digital Seismograph Networks*. https://doi.org/10.7914/SN/HA

University of Memphis. (1982). CERI southern Appalachian seismic network [Dataset]. *International Federation of Digital Seismograph Networks*. Retrieved from http://www.fdsn.org/networks/detail/ET/

15252027, 2024, 7, Downloaded from https://agupubs.onlinelibrary.wiley.com/doi/10.1029/2024GC011559 by Washington University School Of Medicine, Wiley Online Library on [02/05/2025]. See the Terms and Conditions (https://onlinelibrary.wiley.com/terms-and-conditions) on Wiley Online Library for rules of use; OA articles are governed by the applicable Creative Commons License

University of Patras. (2000). University of Patras, seismological laboratory [Dataset]. *International Federation of Digital Seismograph Networks*. https://doi.org/10.7914/SN/HP

University of Puerto Rico. (1986). Puerto Rico seismic network Puerto Rico strong motion program [Dataset]. *International Federation of Digital Seismograph Networks*. https://doi.org/10.7914/SN/PR

University of Southampton. (2013). Trans-Haiti network [Dataset]. *International Federation of Digital Seismograph Networks*. Retrieved from http://www.fdsn.org/networks/detail/ZU_2013/

University of South Carolina. (1987). South Carolina seismic network [Dataset]. *International Federation of Digital Seismograph Networks*. https://doi.org/10.7914/SN/CO

University of the West Indies. (1965). Eastern Caribbean seismograph network [Dataset]. *International Federation of Digital Seismograph Networks*. Retrieved from http://www.fdsn.org/networks/detail/TR/

Vallée, M., Charléty, J., Ferreira, A. M., Delouis, B., & Vergoz, J. (2011). SCARDEC: A new technique for the rapid determination of seismic moment magnitude, focal mechanism and source time functions for large earthquakes using body-wave deconvolution. *Geophysical Journal International*, *184*(1), 338–358. https://doi.org/10.1111/j.1365-246x.2010.04836.x

Various Institutions. (1965). International miscellaneous stations [Dataset]. *International Federation of Digital Seismograph Networks*. https://doi.org/10.7914/VEFQ-VH75

Velasco, A., Kaip, G., Wamalwa, A., & Patlan, E. (2011). Seismic characterization of Menengai crater, Kenya [Dataset]. *International Federation of Digital Seismograph Networks*. https://doi.org/10.7914/SN/1C_2011

Wagner, L. (2012). Pre-hydrofracking regional assessment of central Carolina seismicity [Dataset]. *International Federation of Digital Seismograph Networks*. https://doi.org/10.7914/SN/XQ_2012

Weis, D., Harpp, K. S., Harrison, L. N., Boyet, M., Chauvel, C., Farnetani, C. G., et al. (2023). Earth's mantle composition revealed by mantle plumes. *Nature Reviews Earth & Environment*, *4*(9), 1–22. https://doi.org/10.1029/97JB00395

Wen, L. (2000). Intense seismic scattering near the Earth's core-mantle boundary beneath the Comoros hotspot. *Geophysical Research Letters*, *27*(22), 3627–3630. https://doi.org/10.1029/2000GL011831

Wysession, M., Wiens, D., & Nyblade, A. (2011). Investigation of sources of intraplate volcanism using PASSCAL broadband instruments in Madagascar, the Comores, and Mozambique [Dataset]. *International Federation of Digital Seismograph Networks*. https://doi.org/10.7914/SN/XV_2011

Yu, S., & Garnero, E. J. (2018). Ultralow velocity zone locations: A global assessment. *Geochemistry, Geophysics, Geosystems*, *19*(2), 396–414. https://doi.org/10.1002/2017GC007281

Yuan, K., & Romanowicz, B. (2017). Seismic evidence for partial melting at the root of major hot spot plumes. *Science*, *357*(6349), 393–397. https://doi.org/10.1126/science.aan0760

ZAMG—Zentralanstalt für Meterologie und Geodynamik. (1987). Austrian seismic network [Dataset]. *International Federation of Digital Seismograph Networks*. https://doi.org/10.7914/SN/OE

Zhang, X. J., Parai, R., & Lassiter, J. C. (2024). Primordial and recycled noble gases in the Cook-Austral HIMU mantle: Insights into the onset of volatile subduction. *Earth and Planetary Science Letters*, *629*, 118591. https://doi.org/10.1016/j.epsl.2024.118591

Zhang, X.-Y., Chen, L.-H., Wang, X.-J., Hanyu, T., Hofmann, A. W., Komiya, T., et al. (2022). Zinc isotopic evidence for recycled carbonate in the deep mantle. *Nature Communications*, *13*(1), 6085. https://doi.org/10.1038/s41467-022-33789-6

Zindler, A., & Hart, S. (1986). Chemical geodynamics. *Annual Review of Earth and Planetary Sciences*, *14*(1), 493–571. https://doi.org/10.1146/annurev.ea.14.050186.002425

15252027, 2024, 7, Downloaded from https://agupubs.onlinelibrary.wiley.com/doi/10.1029/2024GC011559 by Washington University School Of Medicine, Wiley Online Library on [02/05/2025]. See the Terms and Conditions (https://onlinelibrary.wiley.com/terms-and-conditions) on Wiley Online Library for rules of use; OA articles are governed by the applicable Creative Commons License